Supplementary Information for Estimating Earth's past field strength from individual sources in archaeological ceramics using Quantum Diamond Microscopy

Ualisson D. Bellon[1*], Gelson F. Souza-Junior[2,4], Wyn Williams[1], Adrian R. Muxworthy[3], Leonardo Uieda[2], Roger R. Fu[4], Ricardo I. F. Trindade[2], and Carolina S. Moraes[2]

[1]School of Geosciences, University of Edinburgh, Edinburgh, EH9 3FE, United Kingdom
[2]Department of Geophysics, Institute of Astronomy, Geophysics and Atmospheric Sciences (IAG), University of São Paulo, São Paulo, 05360020, Brazil
[3]Department of Earth Science and Engineering, Imperial College London, South Kensington Campus, SW7 2AZ, UK
[4]Department of Earth and Planetary Sciences, Harvard University, 20 Oxford St. Geo Museum 204B, United States
[*]*Corresponding author: ualisson.bellon@ed.ac.uk*

Contents

This Supplementary File contains – apart from a complete methodological description of the short methods presented in the manuscript – eight figures (S1–S8). For additional details, please refer to the main manuscript. The contents of this Supplementary File are covered by the same license as the main manuscript, which should be cited when referencing this material.

1 Supplementary Methods

1.1 Magnetic data acquisition

Figure S 1 provides an overview of the complete magnetic data acquisition and processing pipeline used in this paper.

We relied on a ceramic archaeological sample from the Jesuit Missions in Brazil [1]. The sample (RSLG1-03, 1657–1687 AD) is thought to have been fired in a kiln and to have acquired a thermoremanent magnetisation. The fragment used to prepare the thin section was not field-oriented, but it still retained its pristine NRM. We acquired the

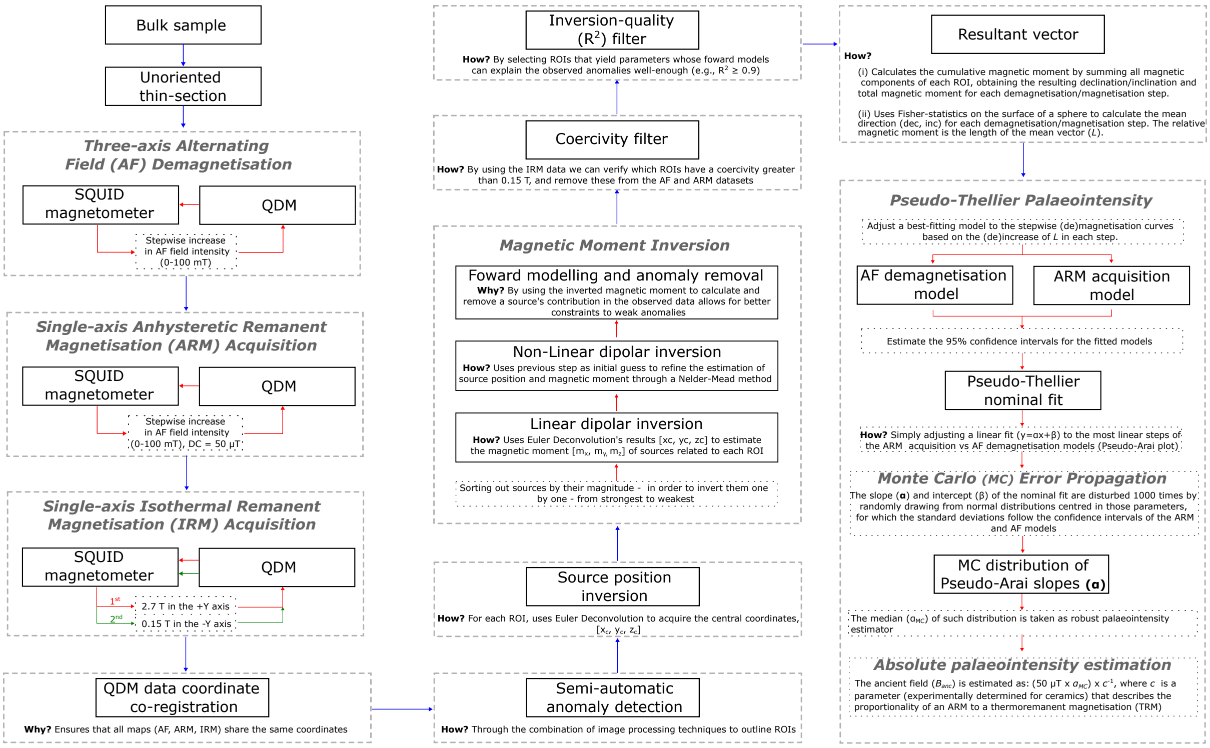

Figure S 1: Workflow of the methodology used in this study. All terms and abbreviations are defined throughout the manuscript. The main processes are connected from left to right, as indicated by the blue arrows, while internal processes are marked by red/green arrows.

three-axis AF (alternating field) demagnetisation curves of the entire thin section using a 2G RAPID Superconducting Rock Magnetometer within a magnetically-shielded room at the Harvard palaeomagnetics Laboratory. Measurements were taken at field intervals of 0 (NRM), 10, 15, 20, 25, 30, 35, 40, 45, 50, 60, 70, 80, 90, and 100 mT. Anhysteretic remanent magnetisations (ARMs) were sequentially acquired at the same field steps (in the positive Y-axis), using a laboratory DC bias field of $B_{\mathrm{lab}} = 50\ \mu$T — a value within the same order of magnitude as classical absolute palaeointensity estimates obtained from sister samples in previous studies ($\approx 47\ \mu$T [1]).

Simultaneously with each AF/ARM step, we measured local microscopic surface magnetic anomalies on the thin section using a Quantum Diamond Microscope (QDM) at the same institution. Two regions exhibiting pronounced concentrations of dipolar anomalies, previously identified in the proof-of-concept study of [2], were selected for this purpose. These regions are hereafter referred to as Map I and Map II. The individual measured areas covered 1410 μm $\times$ 2256 μm, with a grid spacing of 2.35 μm, yielding a total of $N = 576 \times 103$ grid points. Data collection was conducted at a constant sensor-to-sample distance of 1–5 μm, enabling high-resolution mapping of the magnetic field distribution. QDM measurements were performed in projected magnetic microscopy (PMM) mode and subsequently converted to the vertical component of the magnetic field (b_z) using a spectral approach [3–5]. A bias magnetic field of 0.9 mT was applied during acquisition, periodically reversed to yield an effective net bias field of 400 nT. Once both the QDM and bulk measurements have been obtained, we compare them to evaluate the consistency between high-resolution magnetic microscopy data and traditional bulk palaeomagnetic measurements.

Finally, after the ARM acquisition, we imparted isothermal remanent magnetisations (IRMs) using a pulse magnetometer, applying peak DC fields of 2.70 T and 0.15 T in the $+Y$ and $-Y$ directions, respectively. This allows us to assess whether the coercivities of the detected anomalies in the surface maps are greater or lower than the applied fields by examining whether, and to what extent, they align with the field direction. Following each IRM application, both regions were QDM-imaged.

1.2 QDM coordinate system referencing

Adjustment of the mapped region between measurements is typically performed manually during QDM data acquisition. As the inversion method relies on tracking the same magnetic anomalies through stepwise demagnetisation and magnetisation procedures, all maps are required to be aligned to a common coordinate system. This section describes the mathematical approach used to co-register the datasets following acquisition.

Let $I_{\text{ref}}(x, y)$ denote the grayscale LED image acquired during a QDM measurement (in our case, IRM 2.7 T), and $I_i(x, y)$ the LED image recorded during any other step i (either AF or ARM). The goal is to determine a two-dimensional affine transformation $\mathbf{T}_i$ that brings the coordinate system of I_i into that of the reference image I_{ref}, thereby allowing all subsequent QDM maps to be expressed in common spatial coordinates. Each pixel in the image plane is represented by its Cartesian coordinates $\mathbf{p} = [x,\ y,\ 1]^{\mathsf{T}}$, where x and y are pixel coordinates. After alignment, the corresponding location in the reference frame is given by $\mathbf{p}' = [x',\ y',\ 1]^{\mathsf{T}}$.

The mapping between $\mathbf{p}$ and $\mathbf{p}'$ is described by an affine transformation of the form

$$\mathbf{p}' \ = \ \mathbf{H}\,\mathbf{p} \ = \ \begin{bmatrix} a_{11} & a_{12} & t_x \\ a_{21} & a_{22} & t_y \\ 0 & 0 & 1 \end{bmatrix} \begin{bmatrix} x \\ y \\ 1 \end{bmatrix}, \tag{S1}$$

where a_{11} and a_{22} govern scaling along the x and y axes, a_{12} and a_{21} introduce shear and contribute to in-plane rotation, and t_x and t_y encode translations along the respective axes [6, 7]. The matrix $\mathbf{H} \in \mathbb{R}^{3\times 3}$ constitutes the full homogeneous representation of the affine transformation. Because the z-coordinates are a flat surface, we can reduce its representation as

$$\mathbf{T}_i = \begin{bmatrix} \mathbf{A} \mid \mathbf{t} \end{bmatrix} = \begin{bmatrix} a_{11} & a_{12} & t_x \\ a_{21} & a_{22} & t_y \end{bmatrix},$$

so the coordinate transformation simplifies to

$$[x', y']^\mathsf{T} = \mathbf{A}\,[x, y]^\mathsf{T} + \mathbf{t}. \tag{S2}$$

The transformation parameters are obtained from point correspondences between I_i and I_{ref}. A set of keypoints $\mathbf{C}_i = \{(\mathbf{p}_j^{(i)}, \mathbf{p}_j^{(\text{ref})})\}_{j=1}^N$ is first extracted from both images using ORB feature descriptors [8] and matched using Hamming distance [6]. The optimal affine transformation $\mathbf{T}_i$ is then determined by minimising the reprojection error between matched points:

$$\mathbf{T}_i = \arg\min_{\mathbf{T}} \sum_{j \in \mathcal{S}_i} \big\| \mathbf{p}_j^{(\text{ref})} - \mathbf{T}\,\mathbf{p}_j^{(i)} \big\|_2^2, \tag{S3}$$

where $S_i \subseteq \mathbf{C}_i$ is the set of inlier correspondences identified by the RANSAC algorithm [6, 9], i.e., the keypoint pairs whose reprojection error under the estimated affine transformation falls below a predefined tolerance. Once $\mathbf{T}_i$ has been computed from the LED images, it is applied to the magnetic field map $b_{zi}(x, y)$ associated with the same acquisition step. For each point (x', y') in the reference frame, the corresponding value in the aligned map is evaluated at the back-projected coordinates in the original map:

$$b_{zi}^{\text{aligned}}(x', y') = b_{zi}\big(\mathbf{A}^{-1}\big([x', y']^\mathsf{T} - \mathbf{t}\big)\big). \tag{S4}$$

In practice, nearest-neighbor resampling is used during the warping step to preserve the absolute magnitude of the measured field, and pixels that map outside the domain of $b_z i$ are assigned zero values. We also perform an analysis of the distribution of field intensities before and after the alignment proceedure to verify if no computational aberrations were originated, also manually comparing the aligned LEDs to the reference frame. The algorithm is provided in the data repository.

1.3 Magnetic Inversion Data Analysis

Once the QDM maps are aligned, we proceed to invert the magnetic signal. This is achieved using the **A**nomaly **M**apping via **A**utonomous b**Z**-component positioning and **O**ptimized **N**onlinear inversion method [2, 10]. The procedure begins with the detection of surface magnetic anomalies and the delineation of regions of interest (hereafter referred to as “windows”) around them. This is accomplished through a combined calculation of the total gradient anomaly (TGA), followed by a Laplacian of Gaussian (LoG) filter and sequential contrast stretching applied to an upward-continued map. The depth of the equivalent dipolar source is then estimated using a modified Euler deconvolution procedure [2, 10]. This depth estimate provides *a priori* information for the subsequent inversion stage. Finally, the script iteratively inverts the magnetic moment vector in the three Cartesian directions, $\mathbf{m}_i = [m_{x,i},\, m_{y,i},\, m_{z,i}]^{\mathsf{T}}$, where each component represents the contribution of source i along the x-, y-, and z-axes, respectively, within each window.

We begin by identifying all magnetic sources in the IRM 2.7 T dataset and solving for their respective magnetic moments. By applying a strong magnetic pulse at 2.7 T at the end of the measurement sequence, we are able to reveal sources that were not previously saturated. The clear signal from these sources serves as a reliable guide for accurately resolving magnetic directions. The windows coordinates defined in the IRM 2.7 T dataset act as our master ROIs, which are subsequently applied to all other datasets (IRM −0.150 T, AF, and ARM). This ensures that we consistently track the behaviour of the same magnetic anomalies across measurements. As an initial filter, we evaluate the trustworthiness of each ROI in the IRM 2.7 T dataset using the coefficient of determination (R^2), defined as

$$R^2 = 1 - \frac{\sum (d_{\mathrm{obs}} - d_{\mathrm{calc}})^2}{\sum (d_{\mathrm{obs}} - \bar{d}_{\mathrm{obs}})^2}, \tag{S5}$$

where d_{obs} represents the observed magnetic anomaly within each ROI (window), d_{calc} is the corresponding modeled anomaly computed from the inverted magnetic moment, and $\bar{d}_{\mathrm{obs}}$ is the mean of the observed data.

To ensure the reliability of our AF-dependent palaeointensity analysis, it is necessary to apply a coercivity filter. Supplementary Figure S4 shows the window directions used for the coercivity analysis. This is because our method relies on alternating field (AF) demagnetisation, and the maximum applied AF field in our experiments is 100 mT. Any sources with coercivities higher than this value would remain largely unaffected by AF treatment, thereby biasing our results. Identifying and removing these high-coercivity sources is therefore a critical first step. To do this, we exploit the fact that low-coercivity components will reverse their polarity when the sample is magnetised in opposite directions, while high-coercivity components will not. Practically, this means we compare the behaviour of the same windows (ROIs) between two induced remanent magnetisation (IRM) states: one saturated at 2.7 T and another induced in the opposite direction at −0.150 T. By examining the angular difference in their magnetic directions, we can identify sources with coercivities higher than our AF treatment limit.

There are several sources of uncertainty that can lead to a poor fit between observed and modeled data. The most evident cases in our inversions correspond to anomalies that are not well represented by a simple dipolar signal. These are systematically filtered out by applying a coefficient of determination threshold of $R^2 > 0.9$ for data acceptance. First, we remove windows with $R^2 < 0.9$ from the IRM 2.7 T dataset and then remove the same windows from the IRM -0.150 T dataset. Next, we perform the same quality check on the IRM -0.150 T fit, removing any additional windows where $R^2 < 0.9$, and correspondingly discard them from the IRM 2.7 T dataset as well. This ensures that only well-resolved anomalies are retained in both IRM states, allowing a direct and meaningful comparison.

Finally, we apply the coercivity filter (B_{cr}): if the angular distance of a given anomaly has not changed by at least 90° between the IRM 2.7 T and IRM -0.150 T states, it is inferred that its total coercivity exceeds the maximum AF field used (100 mT). Such sources are removed from the dataset, as their presence would compromise the AF-based palaeointensity estimation. All windows eliminated through this filtering process are also excluded from the subsequent AF and ARM dataset analyses.

1.3.1 Recovering the remanence of reliable/well-solved sources

Each anomaly on the b_z QDM map may originate from either the stray field of an individual magnetic particle or from a cluster of particles. Because we are dealing with thermal remanent magnetisation, the magnetic moment of each particle tends to align with the easy axis that is closest to the direction of the ambient magnetic field B_{anc}. However, because the spatial orientation of each particle is not necessarily such that its easy axis lies close to B_{anc}, the resulting moment directions may appear random at the scale of individual anomalies. This apparent randomness does not imply a lack of alignment, but rather alignment to the nearest energetically favorable axis constrained by each particle's anisotropy. Consequently, unless an anomaly reflects the combined signal of a sufficiently large particle cluster—whose cumulative magnetisation can align closely with B_{anc} (see [11])—the directions associated with each ROI should be integrated into a single, bulk magnetic vector.

This can be done by calculating the cumulative magnetic moment from all n sources as the vector sum of their individual moments:

$$\mathbf{M}_{\text{tot}} = \sum_{i=1}^{n} \mathbf{m}_i. \tag{S6}$$

Alternatively, the directional structure of the magnetic moments can be described using directional statistics on the unit sphere, following the Fisher distribution [12]. The dispersion of moment directions is modeled by the Fisher probability density function:

$$P_d(\theta) = \frac{\kappa}{4\pi \sinh \kappa} \exp\big(\kappa \cos\theta\big), \tag{S7}$$

where θ is the angular deviation from the true mean direction, and κ is the concentration (or precision) parameter controlling the angular spread.

Let $\hat{\mathbf{m}}_i$ denote the normalised magnetic moment of source i, i.e.,

$$\hat{\mathbf{m}}_i = \frac{\mathbf{m}_i}{\|\mathbf{m}_i\|} \in \mathbb{R}^3, \quad \text{with} \quad \|\hat{\mathbf{m}}_i\| = 1.$$

The resultant vector of all n unit vectors is defined as

$$\mathbf{L} = \sum_{i=1}^{n} \hat{\mathbf{m}}_i = [m_x,\, m_y,\, m_z]^{\mathsf{T}}, \tag{S8}$$

and its length is given by

$$L = \|\mathbf{L}\| = \sqrt{m_x^2 + m_y^2 + m_z^2}. \tag{S9}$$

The concentration parameter κ is estimated as:

$$\kappa = \frac{n-1}{n-L}, \tag{S10}$$

where L reflects the directional coherence among the sources. Larger values of κ indicate tighter clustering of directions around the mean. Finally, the angular radius of the 95% confidence cone around the mean direction is approximated by:

$$\alpha_{95} = \frac{140^\circ}{\sqrt{\kappa}}. \tag{S11}$$

Note that while $\mathbf{M}_{\text{tot}}$ retains the physical magnitude of each source and thus yields a true net moment, the Fisher-based resultant vector $\mathbf{L}$ encodes only the directional consistency among sources. In this sense, $\mathbf{L}$ serves as a statistical analogue to net moment magnitude, capturing the alignment of source directions independently of their intensities.

In direct absolute palaeointensity experiments, the total magnetic moment $\mathbf{M}_{\text{tot}}$ is essential, as it reflects the net magnetisation strength. However, because our analysis is focused on the relative proportionality of ARM to TRM, the resultant vector length $\mathbf{L}$ becomes more informative. This is particularly important in cases where the magnetisation arises from a mixture of particles with different magnetic moments. For example, if a few large particles dominate the moment distribution, their influence can disproportionately bias $\mathbf{M}_{\text{tot}}$ toward their individual directions, even if most particles are aligned differently. In contrast, the Fisher resultant $\mathbf{L}$ treats all unit vectors equally, thereby eliminating amplitude bias and emphasising directional coherence. This approach is especially advantageous in datasets with limited source counts, where individual particle contributions can otherwise skew the bulk magnetisation direction. By monitoring the variation in $\mathbf{L}$ across AF and ARM steps, we obtain a purely directional measure of relative alignment strength. Moreover, this formulation allows us to propagate directional uncertainty via the confidence angle α_{95}.

Now, for the number of windows used in the Fisher statistics at each AF or ARM step, we apply an additional threshold by considering only those with $R^2 > 0.9$, thereby ensuring high inversion quality. To illustrate the impact of this criterion, we also evaluate lower R^2 thresholds and show how these affect subsequent Pseudo-Thellier palaeointensity estimations.

1.3.2 Pseudo-Thellier palaeointensity estimation

To obtain the palaeointensity, the remaining NRM after each AF demagnetisation step must be plotted against the ARM acquisition at the same step. A linear fit through these segments yields a slope (α). If the magnetic mineralogy and domain state are appropriate, the ancient magnetic field (B_{anc}) responsible for the NRM can be inferred using the following relationship. The Pseudo-Thellier approach [13, 14] is based on:

$$B_{\text{anc}} = \frac{B_{\text{lab}} \cdot |\alpha|}{c}, \tag{S12}$$

where c is a calibration factor used to convert the result into an absolute palaeointensity.

Although one could simply fit the data directly, in our case the limited number of particle windows resulting from our filtering introduces noise at particular steps, which appear as bumps or outliers in either the NRM decay curve or the ARM acquisition. We interpret these deviations as originating from several possible sources, but mostly from poor experimental control—since the vertical positioning is adjusted manually, it is not guaranteed to be exactly the same for each step. As a result, the sample may be measured slightly farther or closer than in previous steps, degrading the signal and leading to over- or underestimation of the moment magnitude (as suggested by the fact that the directions remain stable throughout the AF/ARM routines). As a consequence, rather than using the raw data points directly, we fit continuous curves to the observed data and then construct the Pseudo-Arai plot from those fitted curves. We adjust two functional families: exponential and logarithmic. For the exponential family, we use

$$\mathrm{NRM}(x) = \varepsilon_1 \, e^{-\varepsilon_2 x} + \varepsilon_3, \tag{S13}$$

$$\mathrm{ARM}(x) = \varepsilon_1 \left(1 - e^{-\varepsilon_2 x}\right) + \varepsilon_3, \tag{S14}$$

and for the logarithmic family,

$$\mathrm{NRM}(x) = \varepsilon_1 \, \ln(x+1) + \varepsilon_2 \, x + \varepsilon_3, \tag{S15}$$

$$\mathrm{ARM}(x) = \varepsilon_1 \, \ln(x+1) + \varepsilon_2, \tag{S16}$$

where x is the AF demagnetisation or ARM acquisition step, and ε_i are free fitting parameters. Equations (S13) and (S15) are applied to the NRM decay, whereas Eqs. (S14) and (S16) are applied to the ARM acquisition.

Fitting is carried out using a least-squares procedure with outlier down-weighting to minimize the influence of anomalous steps. At each demagnetisation or acquisition step, the fitted quantity y corresponds to either the normalised NRM decay or the normalised ARM acquisition. The residuals are defined as

$$r_i = y_i - \hat{y}_i, \tag{S17}$$

where y_i are the observed normalised values and $\hat{y}_i$ are the model predictions obtained from the selected fitting function. The residual standard error is estimated as

$$s = \sqrt{\frac{\sum_{i=1}^{N} r_i^2}{N - \phi}}, \tag{S18}$$

where N is the number of steps and ϕ the number of fitted parameters. The standard error of prediction at a given x_j is then

$$\mathrm{SE}(x_j) = s\sqrt{\frac{1}{N} + \frac{(x_j - \bar{x})^2}{\sum_{i=1}^{N}(x_i - \bar{x})^2}}, \tag{S19}$$

with $\bar{x}$ the mean of the step values. The critical value for the 95% confidence interval is taken from the t-distribution,

$$\zeta_{0.975,\nu}, \qquad \nu = N - \phi, \tag{S20}$$

and the bounds of the confidence interval are finally given by

$$y_i^{\text{lower}} = \hat{y}_i - \zeta_{0.975,\nu}\,\text{SE}(x_i), \qquad y_i^{\text{upper}} = \hat{y}_i + \zeta_{0.975,\nu}\,\text{SE}(x_i). \tag{S21}$$

The confidence interval bounds defined in Eq. S21 are directly used to define the symmetric error bars plotted on the Pseudo-Arai diagram, corresponding to the lower and upper uncertainties for each demagnetisation step on both the NRM and ARM axes. The linear segment of the Pseudo-Arai plot is selected between 30 and 70 mT, where both the NRM decay and ARM acquisition curves exhibit approximately linear behaviour. Over this segment, we perform a linear fit, hereafter referred to as the nominal fit, which is required to include at least seven data points within the selected interval. The slope α obtained from this nominal fit provides the parameter used to calculate the palaeointensity according to Eq. S12.

1.3.3 The Monte-Carlo (MC) approach

While the nominal fit provides a single estimate of the Pseudo-Arai slope α, its uncertainty reflects the combined effects of experimental noise, fitting uncertainty, and directional dispersion at each step. To propagate these contributions, we employ a Monte Carlo (MC) simulation framework coupled with orthogonal distance regression, which allows both x- and y-axis uncertainties to be incorporated into the slope estimation.

For each demagnetisation/magnetisation step x_i, the intensity-based uncertainty is derived from the fitted confidence intervals (Eq. S21) as

$$\sigma_{x,i}^{\text{fit}} = \frac{y_{x,i}^{\text{upper}} - y_{x,i}^{\text{lower}}}{2 \times 1.96}, \qquad \sigma_{y,i}^{\text{fit}} = \frac{y_{y,i}^{\text{upper}} - y_{y,i}^{\text{lower}}}{2 \times 1.96}, \tag{S22}$$

assuming approximate normality of the error distribution. A directional uncertainty component is obtained from the angular dispersion $\alpha_{95,i}$ (Eq. S11) as

$$\sigma_{\text{dir},i} = w_\theta\,\hat{y}_i \left(\frac{\alpha_{95,i}}{1.96}\frac{\pi}{180}\right)^2, \tag{S23}$$

where $w_\theta = 0.5$ (arbitrarily chosen) is a weighting factor controlling the contribution of directional uncertainty relative to the intensity-based error. The total uncertainty for each axis is obtained by combining these terms in quadrature,

$$\sigma_{x,i} = \sqrt{(\sigma_{x,i}^{\mathrm{fit}})^2 + (\sigma_{\mathrm{dir},i})^2}, \qquad \sigma_{y,i} = \sqrt{(\sigma_{y,i}^{\mathrm{fit}})^2 + (\sigma_{\mathrm{dir},i})^2}. \tag{S24}$$

For each of N_{MC} realisations, the Pseudo-Arai coordinates are perturbed by sampling from a split-normal distribution centred on the nominal fitted values $(\hat{x}_i, \hat{y}_i)$,

$$x_i^{(j)} \sim \mathcal{SN}(\hat{x}_i, \sigma_{x,i}^-, \sigma_{x,i}^+), \qquad y_i^{(j)} \sim \mathcal{SN}(\hat{y}_i, \sigma_{y,i}^-, \sigma_{y,i}^+), \tag{S25}$$

where σ^- and σ^+ denote the lower and upper standard deviations from the fitted confidence bounds. For each realisation $j = 1, \ldots, N_{\mathrm{MC}}$, a linear model of the form

$$y = \alpha_j x + \beta_j \tag{S26}$$

is fitted using sing orthogonal distance regression (ODR), which accounts for both x and y uncertainties simultaneously. This yields an ensemble $\{\alpha_j, \beta_j\}_{j=1}^{N_{\mathrm{MC}}}$ of slope and intercept estimates. The distribution of α_j values is then summarized statistically. We use the median α_{MC} as a central estimator for the palaeointensities.

1.4 Focused Ion Beam Nanotomography

Serial focused ion beam–scanning electron microscopy (FIB-SEM) imaging was performed on a Helios DualBeam microscope (Thermo Fisher Scientific) using Auto Slice & View 4 at the Brazilian Nanotechnology National Laboratory (LNNano), Brazilian Center for Research in Energy and Materials (CNPEM). We selected a region characterised by a strongly non-dipolar anomaly to verify the origin of the anomalies excluded during data filtering (Figure S 8). For surface scanning electron microscopy–energy-dispersive X-ray spectroscopy (SEM–EDS) analysis, the thin section was coated with gold. Prior to FIB-SEM acquisition, a 2μm platinum protective layer was deposited over the region of interest to protect the sample during ion-beam milling, and carbon strips were applied along the sides of the thin section to reduce charging. Scanning electron microscopy (SEM) Multi-Detector images were used for analysis. The final dataset consisted of 947 serial images acquired at a pixel size of 10 × 10 nm and a nominal slice thickness of 15 nm, corresponding to a voxel size of 10 × 10 × 15 nm. Acquisition was carried out at 30 kV and 400 pA.

Image processing was performed in Python [15, 16]. The SEM Multi-Detector image stack was loaded as individual TIFF slices, and each slice was converted to 32-bit floating-point format and independently min–max normalised to the range 0–1. To reduce noise, a Gaussian filter ($\sigma = 2.0$ pixels) was applied to each slice. Segmentation was then performed independently for each slice by K-means clustering with eight classes ($k = 8$) using the log-transformed filtered pixel intensities. The resulting clusters were reordered from darkest to brightest according to their mean intensity. Classes 5 and 6, corresponding to high-intensity regions interpreted as probable iron oxides, were combined because they showed a recurrent core–rim spatial arrangement, suggesting that they reflected contrast variation within the same phase rather than two distinct phases. Accordingly, class 6 was morphologically dilated with a disk-shaped structuring element of radius 2 pixels, and overlapping class 5 pixels were incorporated into the merged mask. Because the resulting merged masks showed irregular and locally discontinuous boundaries, they were further refined by Gaussian smoothing to reduce jagged boundary noise, followed by Laplacian-based edge detection and Otsu thresholding to extract binary outlines. These edge maps were then dilated and morphologically closed to connect broken segments and seal small gaps, after which the external contours were filled to generate continuous final masks.

Following segmentation and 3D reconstruction, the final mask stack was converted into an STL mesh and subsequently split into disconnected components corresponding to individual particles ($n = 1880$). For each particle, the three principal directions were determined by principal component analysis (PCA) of the external point cloud, defining the maximum, intermediate, and minimum elongation axes. Aspect ratio (AR) was then calculated as minimum/maximum elongation for oblate particles ($AR < 1$) and maximum/minimum elongation for prolate particles ($AR > 1$). Particle orientations were derived from the PCA-defined principal axes, expressed as azimuth and plunge, and visualised using lower-hemisphere, equal-area stereographic projections.

1.5 Micromagnetic modelling

To investigate the remanence states of these particles, we discretised them in Coreform Cubit using linear tetrahedral finite-element meshes. We used a maximum element size of 9 nm to respect the exchange length of magnetite at 20 °C [17]. Unfortunately, micromagnetic modelling of the largest particles in our dataset, some exceeding 2 µm, is computationally too expensive and would require relaxing this exchange-length criterion beyond what we consider reasonable. To investigate the micromagnetic states of the finest particles within the imaged volume, we therefore defined a region of interest near the sample surface, extending to a depth of 5 µm, and retained only particles smaller than 1 µm but larger than 50 nm ($n = 584$). This subset still allows us to assess the expected contribution of the smallest grains to the anomaly measured at the surface.

We modelled the remanence states micromagnetically using MERRILL [18]. For these simulations, we used magnetite parameters at 20 °C, namely the saturation magnetisation M_s, the magnetocrystalline anisotropy constants K_1 and K_2, and the exchange constant A_{ex}. Their values are 4.825×10^5 A/m [19], -1.304×10^4 J/m^3 and -3.154×10^3 J/m^3 [20], and 1.344×10^{-11} J/m [21], respectively. We initialised each model in a random magnetic state and solved for the minimum of the free magnetic energy, thereby obtaining a local energy minimum (LEM) state. Because a grain may have several easy-axis configurations, we performed 50 such simulations for each particle.

We estimated the vertical component of the stray field produced by each grain using a dipolar approximation. The scalar magnetic potential of an isolated multipole of order L in free space scales as $1/h^{L+1}$, where h is the distance from the source. The corresponding field strength, obtained as the gradient of the potential, scales as $1/h^{L+2}$. For a magnetic dipole ($L = 1$), the vertical component of the field at a point directly above the source is:

$$B_z = \frac{\mu_0}{4\pi} \frac{2m}{h^3} \tag{S27}$$

where m is the magnetic moment (A m^2) and h is the perpendicular distance from the grain centroid to the observation point (5 µm above the sample surface). We assumed a purely dipolar stray field, and evaluation at the point directly above each grain. Higher-order multipole contributions, which decay more rapidly with distance, are neglected for this first order approximation.

Two populations of grains are considered. The first comprises the micromagnetically modelled particles, for which the magnetic moment is obtained from the minimum-energy equilibrium state of the simulation as $m = \langle M \rangle \cdot M_s \cdot V$, where $\langle M \rangle$ is the volume-averaged normalised magnetisation, M_s is the saturation magnetisation, and V is the grain volume. The second population consists of particles with grain size exceeding 1 µm located within 5 µm of the sample surface. For these grains, the magnetic moment is estimated from a power-law relationship calibrated on the modelled population:

$$m = a \cdot d^b \tag{S28}$$

where d is the maximum elongation of the grain (µm) and the coefficients a and b are determined by orthogonal distance regression (ODR) in log–log space.

2 Supplementary Figures

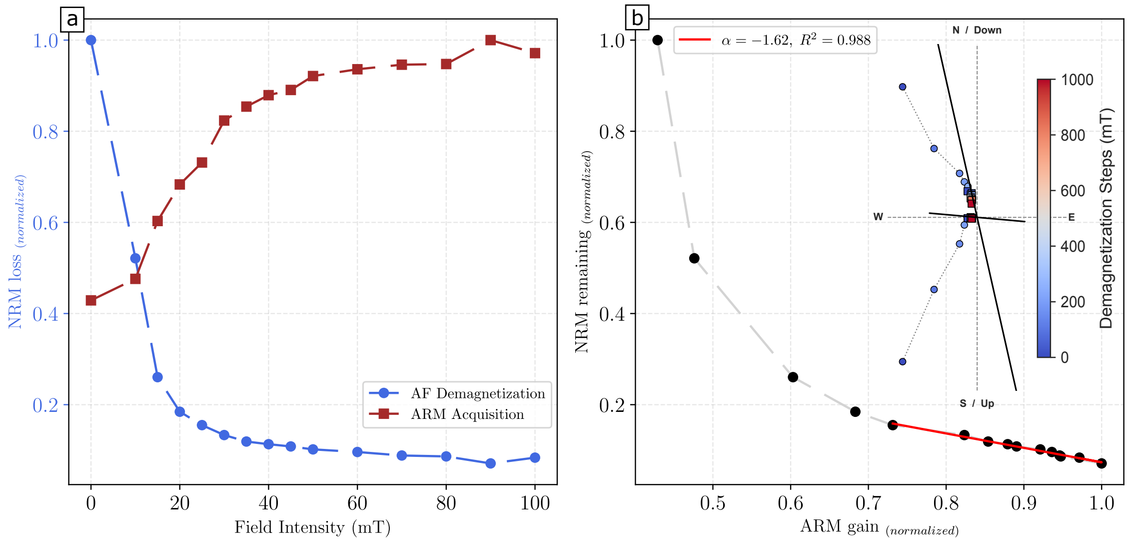

Figure S 2: Pseudo-Thellier protocol measured on the bulk sample. (a) The thin section is stepwise AF (alternating field) demagnetized, and an ARM is imparted at the same steps under a DC (direct current) field of 50 μT. (b) The pseudo-Arai plot (ARM gained vs. NRM remaining) allows us to extract the slope of a linear segment (α), which is then used to calculate the absolute paleointensity. The inset in (b) shows the Zijderveld diagram [22] of the AF demagnetization in (a); squares indicate the points used for principal component analysis (PCA) to determine the characteristic remanent magnetization (ChRM).

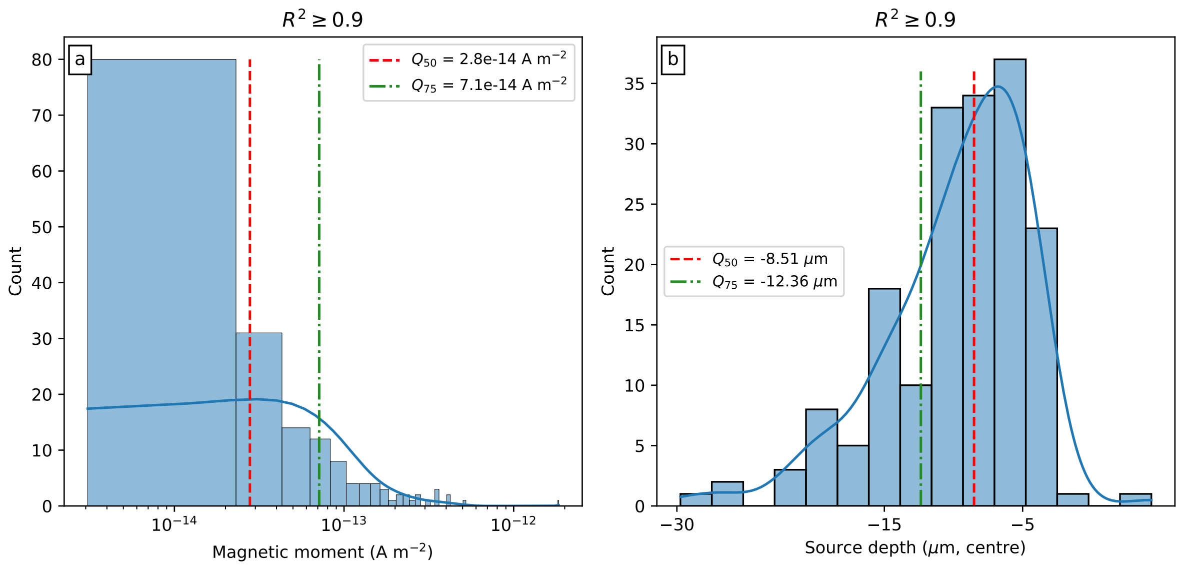

Figure S 3: Magnitude of the magnetic moments (a) and estimated source-center depths (b) inverted from surface quantum diamond microscope data. Results are filtered to include only inversions with $R^2 \geq 0.9$. Solid blue curves represent the kernel density estimates. Red dashed lines indicate the median values (Q_{50}), while green dash–dotted lines denote the upper quartiles (Q_{75}) in each subplot.

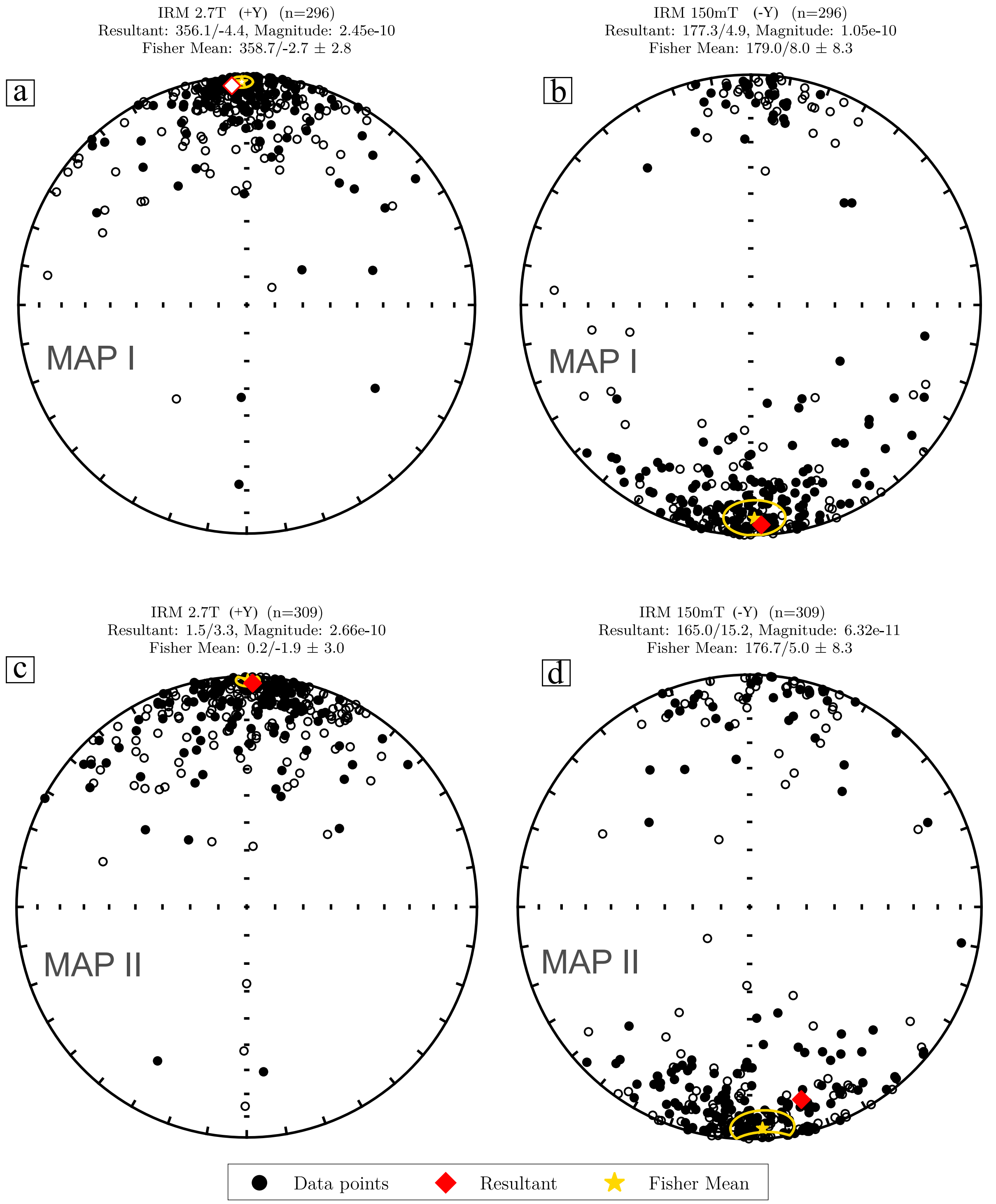

Figure S 4: Directions (declination and inclination) of regions of interest ("windows") inverted after applying isothermal remanent magnetization (IRM) in two opposite polarities (180°), shown in equal-area stereographic projection. (a) A field pulse of 2.7 T is applied in the +Y direction, and (b) a pulse of 150 mT is applied in the opposite (–Y) direction. The data is shown for windows that were well resolved by our inversion method (low residual) for MAP I. Panels (c) and (d) show the corresponding results for MAP II. These directions are used to define the coercivity filter B_{cr}; if the direction is not flipped to the opposite direction within a given angular threshold, the corresponding windows are removed from the alternating-field and anhysteretic remanence datasets. Open(closed) circles for positive (negative) polarities.

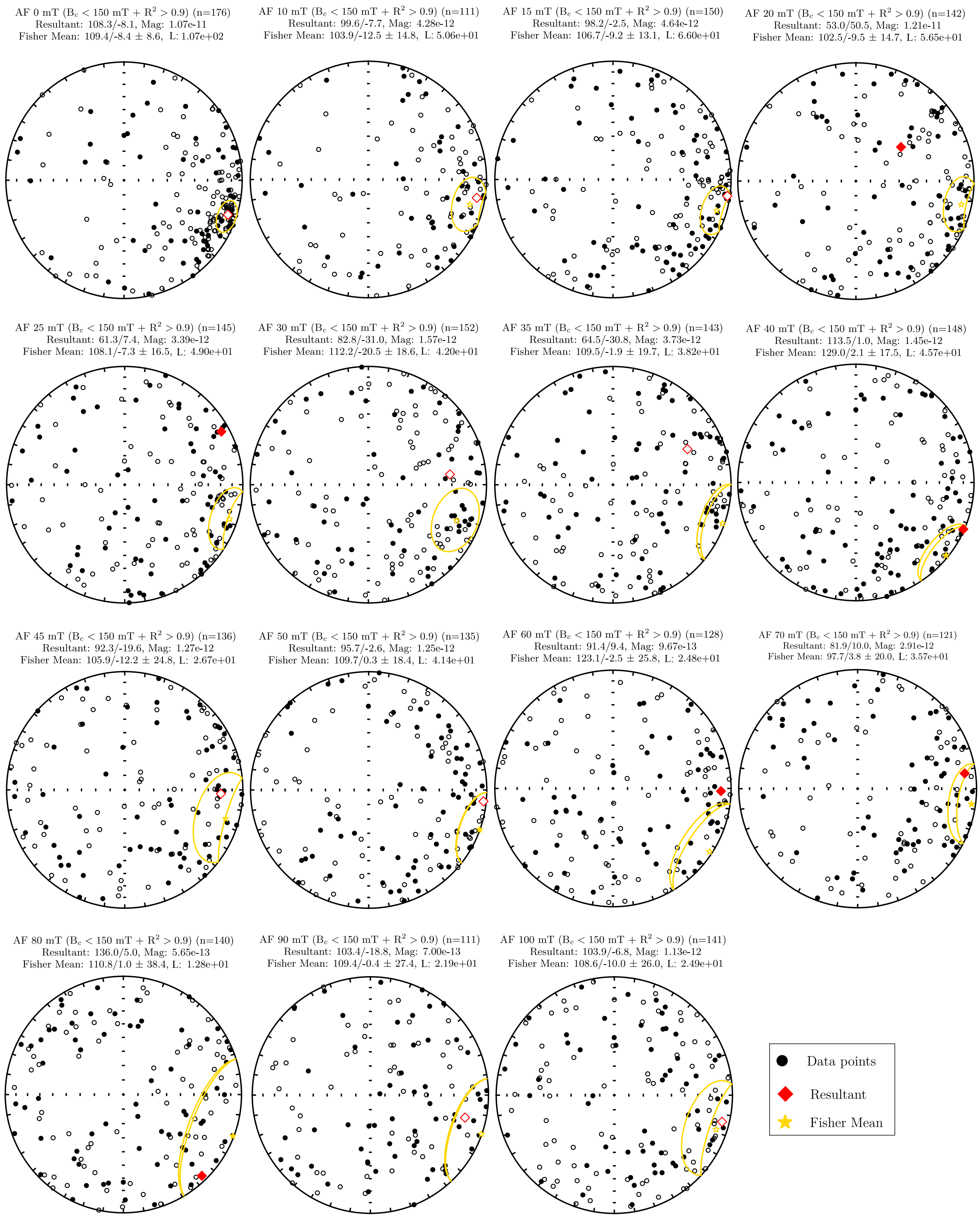

Figure S 5: Inverted magnetic directions from magnetic microscopy data throughout stepwise AF demagnetization, combining datasets from MAP I and MAP II after coercivity (B_{cr}) and coefficient of determination (R^2) filtering. Results are shown as directions (declination/inclination) in equal-area stereographic projection. Open (closed) circles represent positive (negative) polarities.

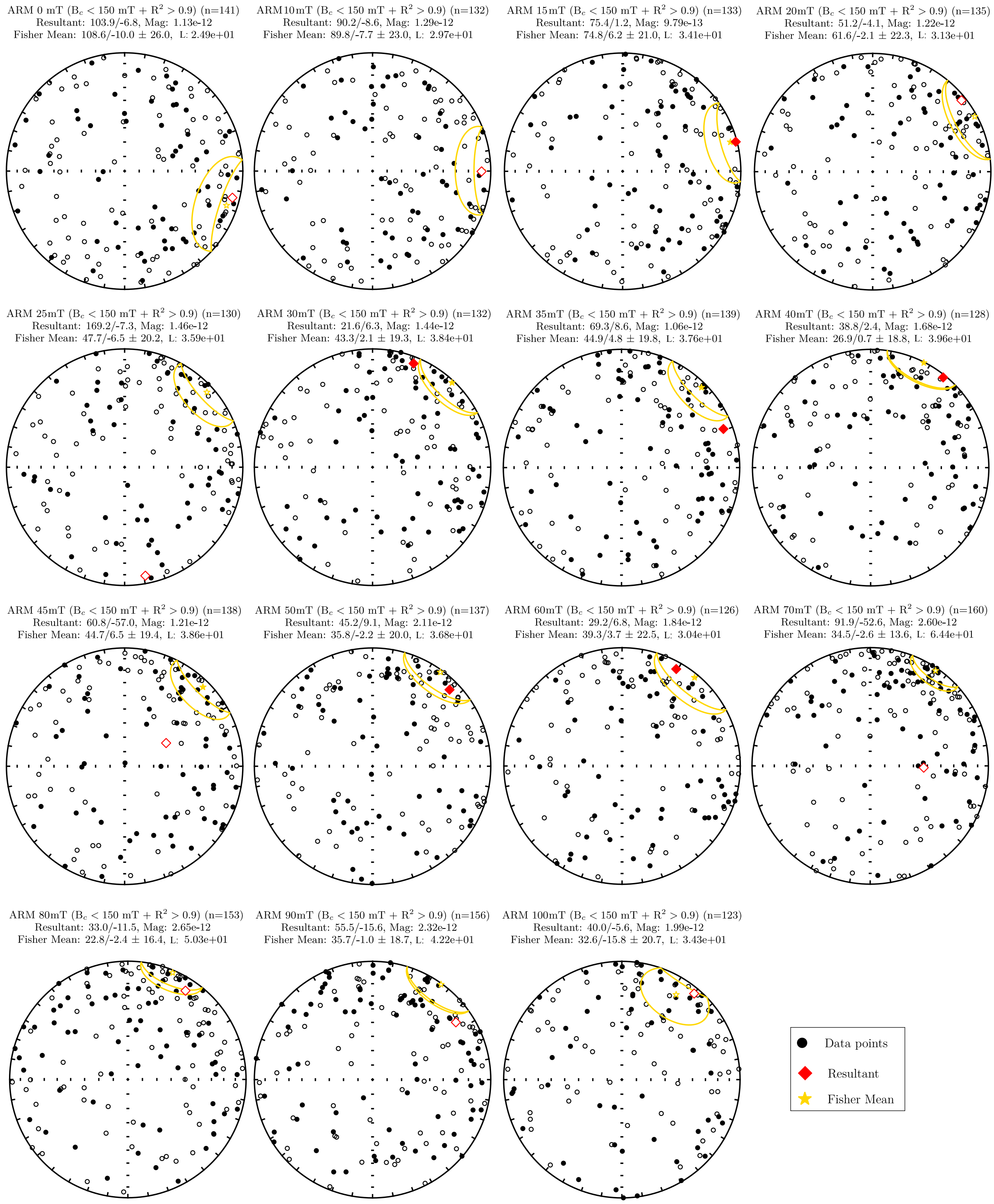

Figure S 6: Inverted magnetic directions from magnetic microscopy data throughout stepwise ARM magnetization (on the same AF fields of Figure 5), combining datasets from MAP I and MAP II after coercivity (B_{cr}) and coefficient of determination (R^2) filtering. Results are shown as directions (declination/inclination) in equal-area stereographic projection. Open (closed) circles represent positive (negative) polarities.

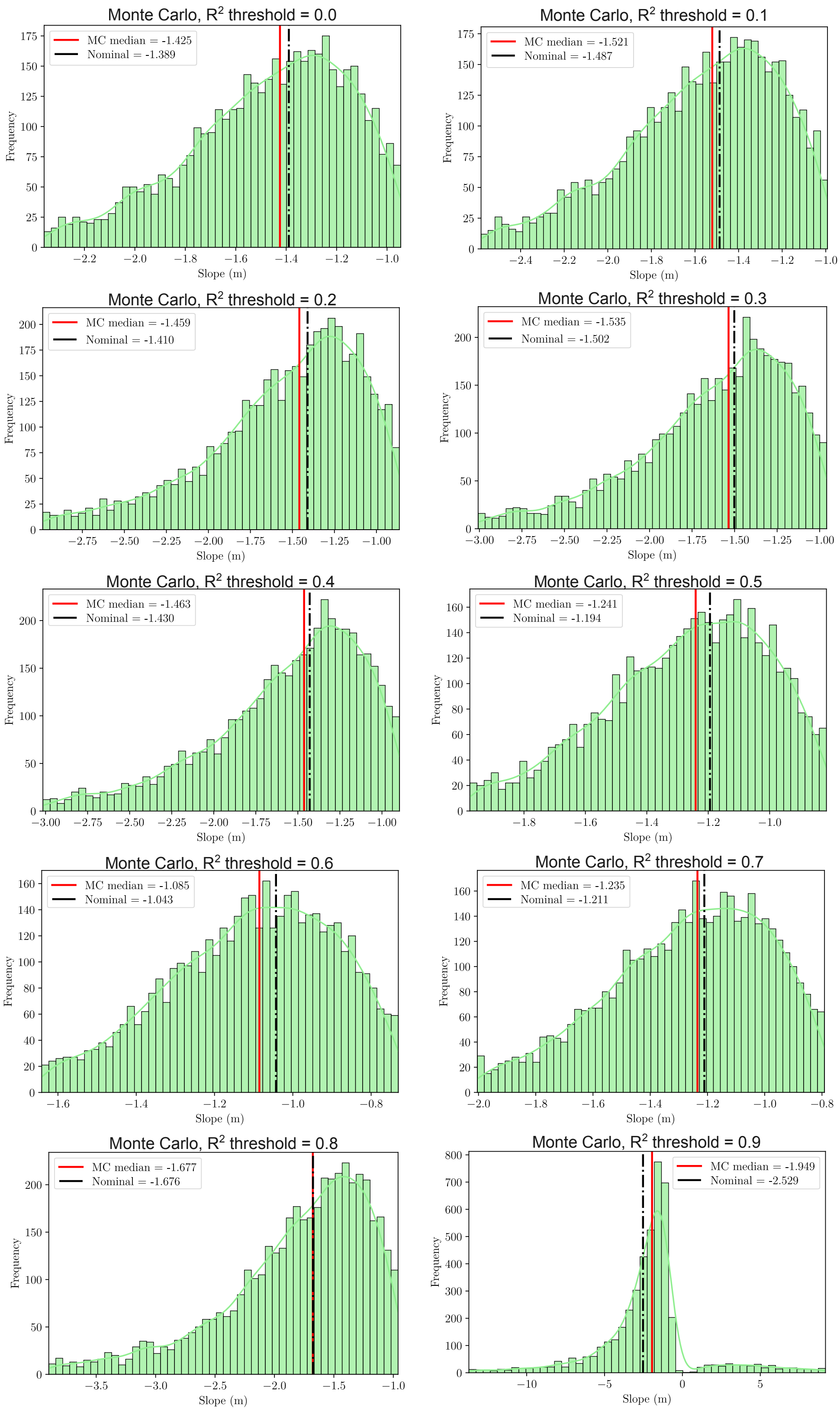

Figure S 7: Monte Carlo evaluation of pseudo-Thellier paleointensity slopes as a function of the minimum R^2 threshold. For each threshold value (0.0–0.9, in steps of 0.1), synthetic pseudo-Arai datasets are generated by perturbing the fitted AF and ARM curves within their confidence bounds and adding a directional term based on the angular dispersion. Each panel shows the resulting distribution of slopes α obtained from orthogonal distance regression over the selected linear window. The central tendency of each distribution (median) is used as a slope estimate for calculating the absolute paleointensity.

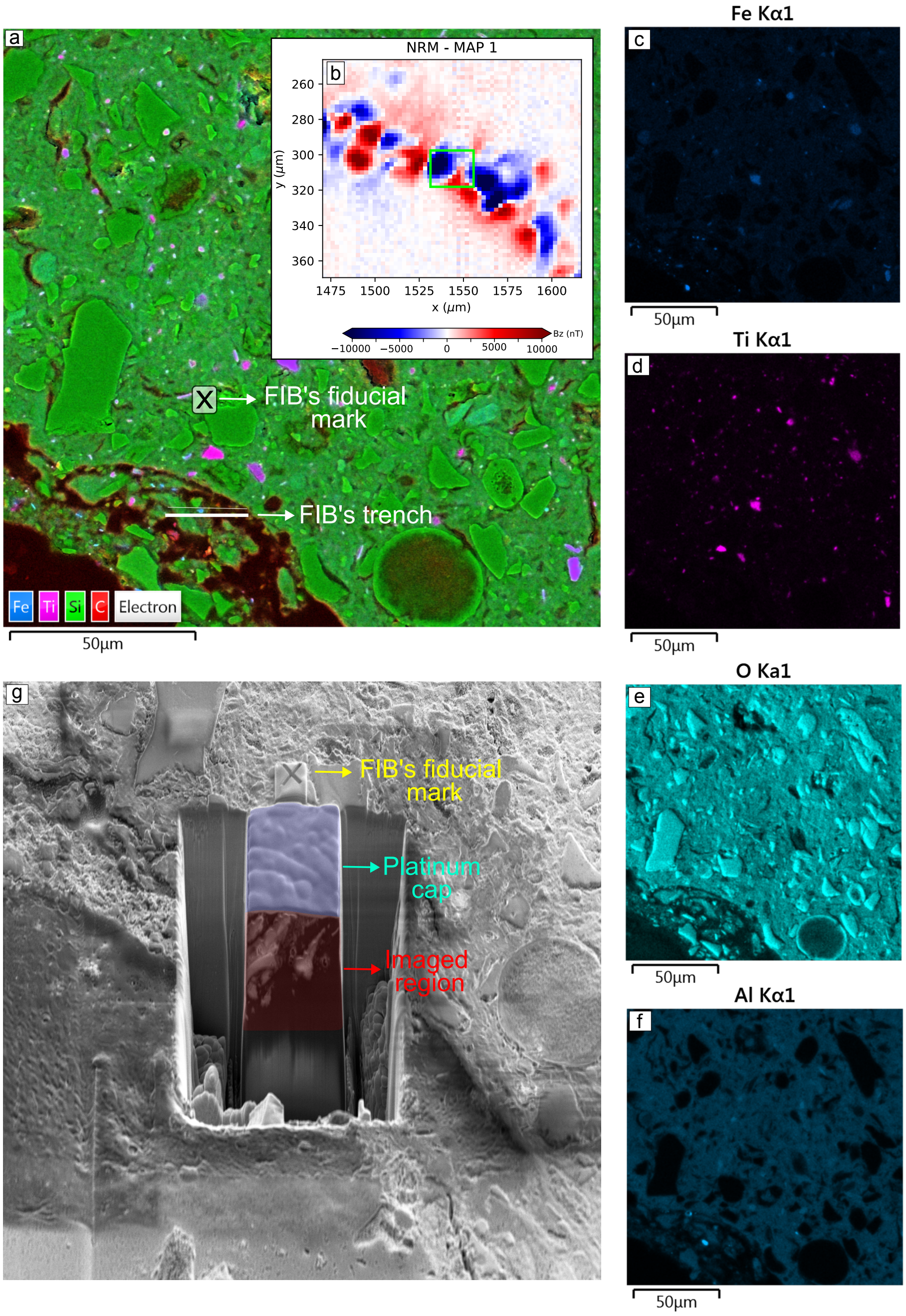

Figure S 8: Focused Ion Beam (FIB) tomography setup. (a) Scanning electron microscopy coupled with energy-dispersive spectroscopy (SEM-EDS) of the region of interest, approximately marked by the green square in the QDM map in (b). Note that this position in the QDM map is only approximate. Panels (c), (d), (e), and (f) show compositional maps for Fe, Ti, O, and Al, respectively. In (g), the tomography setup is visible, where the FIB fiducial mark can be identified relative to the one in (a). The protective platinum cap is highlighted in blue, and the FIB-imaged region is shown in red.

Supplementary References

1. Poletti, W., Trindade, R. I., Hartmann, G. A., Damiani, N. & Rech, R. M. Archeomagnetism of Jesuit Missions in South Brazil (1657–1706 AD) and assessment of the South American database. *Earth and Planetary Science Letters* **445,** 36–47. ISSN: 0012-821X. https://www.sciencedirect.com/science/article/pii/S0012821X16301625 (2016).

2. Souza-Junior, G. F. *et al.* Robust Directional Analysis of Magnetic Microscopy Images Using Non-Linear Inversion and Iterative Euler Deconvolution. *Journal of Geophysical Research: Solid Earth* **131.** e2025JB031725 2025JB031725, e2025JB031725. eprint: https://agupubs.onlinelibrary.wiley.com/doi/pdf/10.1029/2025JB031725. https://agupubs.onlinelibrary.wiley.com/doi/abs/10.1029/2025JB031725 (2026).

3. Lima, E. A. & Weiss, B. P. Obtaining vector magnetic field maps from single-component measurements of geological samples. *Journal of Geophysical Research: Solid Earth* **114.** eprint: https://agupubs.onlinelibrary.wiley.com/doi/pdf/10.1029/2008JB006006. https://agupubs.onlinelibrary.wiley.com/doi/abs/10.1029/2008JB006006 (2009).

4. Glenn, D. R. *et al.* Micrometer-scale magnetic imaging of geological samples using a quantum diamond microscope. *Geochemistry, Geophysics, Geosystems* **18,** 3254–3267. eprint: https://agupubs.onlinelibrary.wiley.com/doi/pdf/10.1002/2017GC006946. https://agupubs.onlinelibrary.wiley.com/doi/abs/10.1002/2017GC006946 (2017).

5. Fu, R. R. *et al.* Weak Magnetic Fields in the Outer Solar Nebula Recorded in CR Chondrites. *Journal of Geophysical Research: Planets* **125.** e2019JE006260 2019JE006260, e2019JE006260. eprint: https://agupubs.onlinelibrary.wiley.com/doi/pdf/10.1029/2019JE006260. https://agupubs.onlinelibrary.wiley.com/doi/abs/10.1029/2019JE006260 (2020).

6. Bradski, G. The OpenCV Library. *Dr. Dobb's Journal of Software Tools* (2000).

7. Gonzalez, R. C. & Woods, R. E. *Digital Image Processing* 4th ed. ISBN: 978-1-292-22304-9 (Pearson Education Limited, 2018).

8. Rublee, E., Rabaud, V., Konolige, K. & Bradski, G. *ORB: An efficient alternative to SIFT or SURF* in *2011 International Conference on Computer Vision* (2011), 2564–2571.

9. Fischler, M. A. & Bolles, R. C. in *Readings in Computer Vision* (eds Fischler, M. A. & Firschein, O.) 726–740 (Morgan Kaufmann, San Francisco (CA), 1987). ISBN: 978-0-08-051581-6. https://www.sciencedirect.com/science/article/pii/B9780080515816500702.

10. Souza-Junior, G. F., Uieda, L., Trindade, R. I. F., Carmo, J. & Fu, R. Full Vector Inversion of Magnetic Microscopy Images Using Euler Deconvolution as Prior Information. *Geochemistry, Geophysics, Geosystems* **25.** e2023GC011082 2023GC011082, e2023GC011082. eprint: https://agupubs.onlinelibrary.wiley.com/doi/pdf/10.1029/2023GC011082. https://agupubs.onlinelibrary.wiley.com/doi/abs/10.1029/2023GC011082 (2024).

11. Bellon, U. D. *et al.* Efficiency of Thermoremanent Magnetization Acquisition in Vortex-State Particle Assemblies. *Geophysical Research Letters* **52.** e2025GL114771 2025GL114771, e2025GL114771. eprint: https://agupubs.onlinelibrary.wiley.com/doi/pdf/10.1029/2025GL114771. https://agupubs.onlinelibrary.wiley.com/doi/abs/10.1029/2025GL114771 (2025).

12. Fisher, R. A. Dispersion on a sphere. *Proceedings of the Royal Society of London. Series A. Mathematical and Physical Sciences* **217,** 295–305 (1953).

13. Stephenson, A. & Collinson, D. Lunar magnetic field palaeointensities determined by an anhysteretic remanent magnetization method. *Earth and Planetary Science Letters* **23,** 220–228. ISSN: 0012-821X. https://www.sciencedirect.com/science/article/pii/0012821X74901964 (1974).

14. Tauxe, L., Pick, T. & Kok, Y. S. Relative paleointensity in sediments: A Pseudo-Thellier Approach. *Geophysical Research Letters* **22,** 2885–2888. eprint: https://agupubs.onlinelibrary.wiley.com/doi/pdf/10.1029/95GL03166. https://agupubs.onlinelibrary.wiley.com/doi/abs/10.1029/95GL03166 (1995).

15. Van der Walt, S. *et al.* scikit-image: image processing in Python. *PeerJ* **2,** e453. https://doi.org/10.7717/peerj.453 (2014).

16. Harris, C. R. *et al.* Array programming with NumPy. *Nature* **585,** 357–362. https://doi.org/10.1038/s41586-020-2649-2 (2020).

17. Rave, W., Fabian, K. & Hubert, A. Magnetic states of small cubic particles with uniaxial anisotropy. *Journal of Magnetism and Magnetic Materials* **190,** 332–348. ISSN: 0304-8853. https://www.sciencedirect.com/science/article/pii/S030488539800328X (1998).

18. Ó Conbhuí, P. *et al.* MERRILL: Micromagnetic Earth Related Robust Interpreted Language Laboratory. *Geochemistry, Geophysics, Geosystems* **19,** 1080–1106. eprint: https://agupubs.onlinelibrary.wiley.com/doi/pdf/10.1002/2017GC007279. https://agupubs.onlinelibrary.wiley.com/doi/abs/10.1002/2017GC007279 (2018).

19. Pauthenet, R. & Bochirol, L. Aimantation spontanee des ferrites. *Journal de Physique et le Radium* **12,** 249–251. https://doi.org/10.1051/jphysrad:01951001203024900 (1951).

20. Fletcher, E. J. & O'Reilly, W. Contribution of Fe2+ ions to the magnetocrystalline anisotropy constant K1 of Fe3-xTixO4. *Journal of Physics C: Solid State Physics* **7,** 171. https://doi.org/10.1088/0022-3719/7/1/024 (Jan. 1974).

21. Heider, F. & Williams, W. Note on temperature dependence of exchange constant in magnetite. *Geophysical Research Letters* **15,** 184–187. eprint: https://agupubs.onlinelibrary.wiley.com/doi/pdf/10.1029/GL015i002p00184. https://agupubs.onlinelibrary.wiley.com/doi/abs/10.1029/GL015i002p00184 (1988).

22. Zijderveld, J. D. A. in *Methods in Palaeomagnetism* (eds Runcorn, S. K., Creer, K. M. & Collinson, D. W.) 254–286 (Elsevier, Amsterdam, 1967).